Unoccupied electronic structure of actinide dioxides

J. G. Tobin [1,*] H. Ramanantoanina [2] C. Daul,[3] P. Roussel [4] S.-W. Yu,[5] S. Nowak,[6] R. Alonso-Mori,[6]
T. Kroll,[6] D. Nordlund,[6] T.-C. Weng,[6] and D. Sokaras[6]

[1]*University of Wisconsin-Oshkosh, Oshkosh, Wisconsin 54901, USA*
[2]*Department of Chemistry, Johannes Gutenberg University Mainz, 55099 Mainz, Germany*
[3]*Department of Chemistry, University of Fribourg, Fribourg, Switzerland*
[4]*Atomic Weapons Establishment (AWE) plc, Aldermaston, Reading, Berkshire RG7 4PR, United Kingdom*
[5]*Lawrence Livermore National Laboratory (LLNL), Livermore, California 94550, USA*
[6]*Stanford Linear Accelerator Center (SLAC) National Accelerator Laboratory, Menlo Park, California 94025, USA*

Ligand field density functional theory calculations of the dioxides of thorium, uranium, and plutonium have been combined with high-energy-resolution fluorescence detection (HERFD) in x-ray absorption spectroscopy and inverse photoelectron spectroscopy (IPES) measurements to provide powerful insight into the underlying composition of the unoccupied $5f$ electronic structure in these $5f$ localized systems. Fine structure in the $5f_{5/2}$ transitions in HERFD can be directly correlated with the fine structure in the leading edge of the IPES. The shapes, intensities, and systematics in HERFD and IPES are explained in a consistent and rigorous fashion in terms of the j-specific $5f$ electronic structure.

I. INTRODUCTION

While actinides are invariably avoided and often detested, they are an immensely important part of modern technological societies [1,2]. For example, there is the value of the electrical power supplied by nuclear fuel. Many countries have a significant fraction of their power grid underpinned by nuclear power, e.g., the United States (∼20%), France (∼75%), and Sweden (∼40%) [3]. Uranium dioxide is the most widely used form of nuclear fuel for the generation of electricity [4], and mixed oxides of U and Pu are often proposed as future fuels. In an era where a major goal is the reduction of the carbon footprint in energy production, nuclear power remains an important option. Furthermore, even if one were to stipulate the immediate elimination of all nuclear power generation, there remains the issue of legacy: nuclear clean-up and storage [5]. Thus, a fundamental and deep understanding of the actinides and their oxides is critically important. However, despite almost a century of effort, the nature of $5f$ electronic structure remains poorly understood and an obstacle to a full understanding of the actinides and the prediction of their behavior, for example, within long-term storage.

The reasons for this delay are intertwined and related. The actinides are radioactive, chemically reactive, biologically toxic, and very complicated [6–9]. For example, elemental Pu has six solid phases, and the face-centered cubic phase is not the most dense [8–10]. Early spectroscopic studies by Lam *et al.* [11] and Veal *et al.* [12] looked at the actinide dioxides. One advantage of those studies was the improvement in terms of chemical stability and surface lifetime over the elemental

forms. Another was the consistency in cross-elemental comparisons since all were dioxides. That philosophy has been applied here.

The actinide dioxides and their related compounds have been the subject of many previous studies, for example, PuO_2 and its nonmagnetic ground state [13], the x-ray photoelectron spectroscopy and its simulation for UO_2, NpO_2, and PuO_2 [14], the high-resolution x-ray absorption measurements and simulations of compounds in the higher oxidation state of U(VI) such as UO_3 [15], and the issue of $5f$ covalency and spin-orbit splitting in actinide dioxides (Th, Pa, U, Np, Pu, and Am) using the screened hybrid density functional model [16,17]. However, in this paper, a different approach has been taken, emphasizing spectral simulations of the actinide dioxides that include effects such as $5f$ cross-sections and angular momentum coupling as well as spin-orbit splitting. The total angular momentum coupling is the key to explaining the fine structure observed in the leading edge of the inverse photoelectron spectroscopy (IPES) spectra, as will be discussed below.

Thorium, uranium, and plutonium each form a dioxide with a fluorite structure, having lattice constants of 5.60, 5.47, and 5.40 Å, respectively [18–21]. This permits a cross comparison of Th^{4+} $(5f^0)$, U^{4+} $(5f^2)$, and Pu^{4+} $(5f^4)$ in very similar chemical environments. In each case, a nine-atom cluster has been used: ThO_8^{12-}, UO_8^{12-}, and PuO_8^{12-} [22]. The actinide is sitting in a site with cubic (octahedral) symmetry, reduced from the spherical symmetry of the free atom or ion. It also allows the comparison of simple, localized systems with only minimal further mixing from effects such as $5f$ delocalization, magnetization, or other complications. This approach permits the utilization of the intermediate coupling model [23–26] both as a check for internal consistency and

_____
*tobinj@uwosh.edu

the prediction of the $5f$ occupation. The importance of this approach will be seen below. While the intermediate coupling model has provided insight into the progressive filling of the $5f$ levels in localized systems in the light actinides, it has not provided any detail concerning the $5f$ density of states (DOS) nor the effects of filling upon the $5f$ DOS. It is that problem which is addressed here.

The cases of the dioxides thus provide a bit of a simplification relative to their elemental forms. While the oxides have actinide configurations, in the ionic limit of Th^{4+} ($5f^0 spd^0$), U^{4+} ($5f^2 spd^0$), and Pu^{4+} ($5f^4 spd^0$), the elemental configurations are Th ($5f^0 spd^4$), U ($5f^3 spd^3$), and Pu ($5f^5 spd^3$) [24–26]. Moreover, while the Th $5f$ states are empty, the elemental U $5f$ states tend toward itinerancy, and the elemental Pu $5f$ states balance on the knife edge between itinerancy and localization [24–26]. This raises the important question of $5f$ duality and electron correlation [27–36]. By choosing to examine the oxides, the impact of these very difficult aspects of $5f$ electronic structure can be minimized. By working in a fairly localized limit, this approach allows the resolution of more simplified cases without addressing the full complexity of $5f$ electronic structure. Furthermore, by concentrating on the simplified limit of localized, highly symmetric systems, it is possible to isolate the importance of the angular momentum coupling in the peak shapes and the strong connection between IPES [37–40] and high-energy-resolution fluorescence detection (HERFD) [41–44]. Success in this regime will be a foundation for addressing the more complex systems later.

On a broad scale, conventional x-ray absorption spectroscopy (XAS) and branching ratio (BR) analyses have all shown the dominance of the total angular momentum effects [23–26]. Cowan's code, which has been the historical foundation for these analyses, is atomic. This effort, using ligand field density functional theory (LFDFT), seeks to go from the atomic picture to a cluster model, including nearest neighbor effects. These issues are addressed in this paper. Moreover, the comparisons herein are therefore not direct comparisons between spectra and DOS but rather spectral simulations vs the spectral measurements, with the spectral simulations providing insight into the underlying DOS, with angular momentum coupling being a key element of the broadening when the number of $5f$ electrons is >0.

Thus, the results of our study are presented here, in Fig. 1. In this paper, we combine a powerful computational approach [22] and detailed spectroscopic measurements using both IPES [37–40] and HERFD [41–44] in XAS to probe the unoccupied electronic structure of ThO_2, UO_2, and PuO_2. This LFDFT can not only explain the j-specific transitions of the HERFD of the UO_2 but also the fine structure observed on the leading edge of both the UO_2 and PuO_2 IPES. Note that each step in the leading edge of both IPES spectra is reproduced by the LFDFT. The systematics of the progressive filling of the light actinides, Th^{4+} ($5f^0$), U^{4+} ($5f^2$), and Pu^{4+} ($5f^4$), is also observed and resolved. A systematic and consistent picture or the $5f$ unoccupied electronic structure is thus obtained.

The remainder of the paper is organized as follows: first, the computational and experimental details will be discussed; then further supporting materials will be presented; and finally, there will be a summary and conclusions.
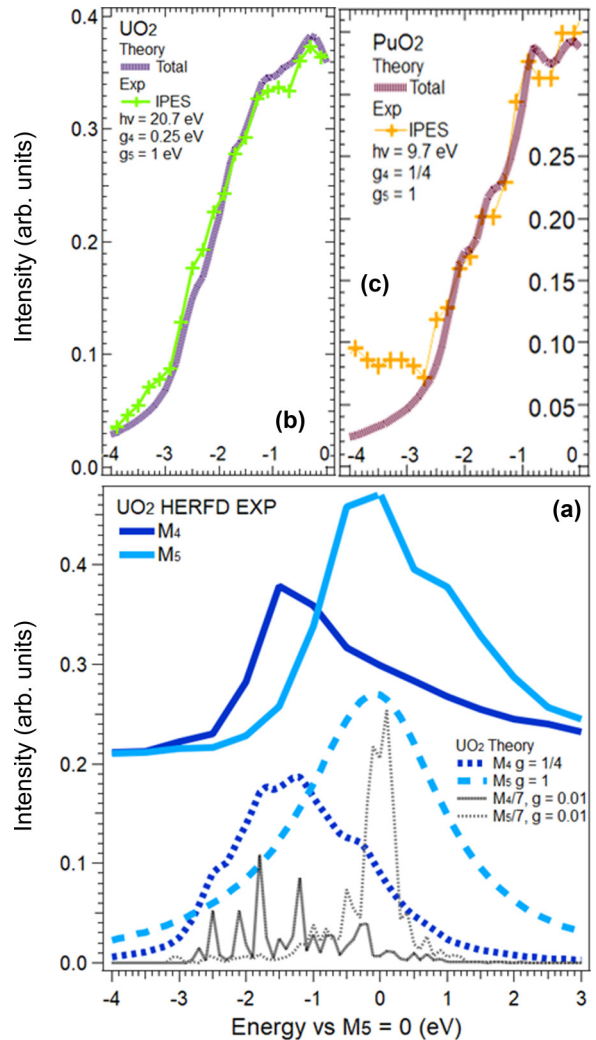

FIG. 1. (a)–(c) The results of the ligand field density functional theory (LFDFT) calculations for UO_8^{12-} and PuO_8^{12-} clusters; (a) the high-energy-resolution fluorescence detection (HERFD) x-ray absorption spectroscopy (XAS) results for UO_2 [34]; and (b) and (c) the inverse photoelectron spectroscopy (IPES) of UO_2 and PuO_2. All panel horizontal axes are energies vs $M_5 = 0$ eV, as discussed in the text. The PuO_2 IPES is at $h\nu = 9.7$ eV [23]. The UO_2 IPES is at $h\nu = 20.7$ eV and from Ref. [25], which also agrees very well with the UO_2 IPES at $h\nu = 9.7$ eV [22]. To better match the experiments, the theory curves were convoluted with Lorenztians to simulate lifetime broadening. The experimental curves were scaled and shifted to match the theory. The value g is the half-width at half maximum of the Lorentzian. See legends and text for details.

II. COMPUTATIONAL AND EXPERIMENTAL

The electronic structures of actinide coordination compounds are often very challenging to obtain [45]. Actinide ions are prone to open-shell species and near-degeneracy correlation, in as much as the theoretical model requires a multireference algorithm and configuration interaction. Post-Hartree-Fock methods, including many-body treatment of electron correlation effects, have been largely developed for dealing with the coordination compounds. For instance, complete active space self-consistent field and

related methodologies currently enjoy wide popularity in computational chemistry [46,47]. They also have limitations: the configuration interaction expansion increases exponentially with respect to the number of active electrons and orbitals, and the calculation of large systems becomes difficult. It is in this context that density functional theory (DFT) is of interest. Kohn-Sham DFT is mainly applied for ground state electronic structures [48]. Its scope includes calculation of large-sized molecules as well as condensed matter. In DFT, excited states are often approached via linear response theory, as it is implemented in the time-dependent DFT (TDDFT) formalism [49]. The disadvantage of TDDFT, however, is that it lacks computational protocols for addressing highly correlated electrons or relativistic spin-orbit coupling, interactions which are very relevant in actinide chemistry. LFDFT is a theoretical method aimed at solving multiplet structure by using DFT, with many applications to lanthanide and actinide systems [22,50]. In LFDFT, near-degeneracy correlation is explicitly treated using an ad hoc configuration interaction algorithm within the active space of Kohn-Sham molecular orbitals [22,50]. The DFT calculations are performed with the average-of-configuration method, insofar as statistically averaged electron density is constructed that is isomorphic with the basis of a model Hamiltonian for a configuration system with actinide $5f$ electrons. The model Hamiltonian is defined so that the most relevant quantum-chemical interactions are considered, including the interelectron repulsion, relativistic spin-orbit coupling, and ligand-field potential, which are entirely derived from the DFT calculation [22,50]. Thus, LFDFT is completely from first principles, thereby very suitable for this paper.

LFDFT calculations have been used to model the actinide $M_{4,5}$ x-ray absorption near edge structure in ThO_2, UO_2, and PuO_2. These transitions are characterized by the promotion of one electron from the core $3d$ orbitals of Th$\sim^{4+}$, U$\sim^{4+}$, and Pu$\sim^{4+}$ to the valence $5f$. The model describes the procedure to resolve nonempirically the multiplet energy levels originating from the two-open-shell system with d and f electrons and to calculate the oscillator strengths corresponding to the dipole-allowed $3d^{10}\,5f^n \rightarrow 3d^9\,5f^{n+1}$ transitions appropriate to represent the d electron excitation process, where n is 0, 2, and 4 for Th, U, and Pu, respectively (n is the $5f$ occupation). In the first step, DFT calculations were performed for the small molecular cluster ThO_8^{12-}, UO_8^{12-}, and PuO_8^{12-} with octahedral symmetry, where the actinide-oxygen bond distances were adjusted to the experimental bond length in the fluorite lattice structures. Furthermore, a series of point charges is placed at the coordinates of the next neighboring actinide and oxygen ions to mimic the long-range interaction of the crystal host. The DFT calculations have been carried out by using the Amsterdam Density Functional program package [51]. The hybrid B3LYP functional [52] was used to compute the electronic structure in line with previous work [22]. Also, in line with previous work, the average of configuration electronic structure is selected to represent the open-shell $3d$ and $5f$ orbitals of the actinide ions. The molecular orbitals were expanded using multiple-zeta Slater-type orbitals with polarization function QZ4P for the actinide atoms and TZP for oxygen [53]. All the calculations have been done at the scalar zeroth-order regular approximation (ZORA) of the relativistic

TABLE I. Some of the details about the calculations, including the calculated ligand-field parameters, interelectron integrals, and spin-orbit coupling constants (in electronvolts). See also Ref. [50] for the explanation of the parameter notations and values.

	ThO_8^{12-}	UO_8^{12-}	PuO_8^{12-}
Configuration average energy			
$\Delta E_{av}(3d, 5f)$	3429.70	3636.40	3872.80
Slater-Condon integrals			
$F^2(5f, 5f)$	5.5009	5.7653	5.9336
$F^4(5f, 5f)$	3.5602	3.7706	3.8516
$F^6(5f, 5f)$	2.6010	2.7687	2.8204
$G^1(3d, 5f)$	1.2874	1.5463	1.6286
$G^3(3d, 5f)$	0.7758	0.9334	0.9913
$G^5(3d, 5f)$	0.5421	0.6525	0.6953
$F^2(3d, 5f)$	1.6488	1.9566	2.0910
$F^4(3d, 5f)$	0.7642	0.9164	0.9789
Spin-orbit coupling constants			
$\zeta(3d)$	63.4881	70.0921	78.0268
$\zeta(5f)$	0.1300	0.1928	0.2230
Ligand-field potential			
B_0^4	−1.5280	−1.2674	−1.1680
B_0^6	0.3307	0.3526	0.3656

Dirac equation level of theory [54], and spin-orbit coupling interaction was introduced by using the spin-orbit ZORA relativistic model. The model of the optical properties due to the actinide $3d^{10}\,5f^n \rightarrow 3d^9\,5f^{n+1}$ transitions has been addressed by means of electronic structure calculations based on the ligand field concept emulating the Slater-Condon integrals, the spin-orbit coupling constants, and the parameters of the ligand field potential needed by the ligand field Hamiltonian from DFT [22]. Some of the calculational parameters are shown in Table I.

As an internal test of computational accuracy, the spectral intensity calculations have been summed to produce predictions of the BR in XAS, where $BR = I_{3d5/2}/(I_{3d5/2} + I_{3d3/2})$, as defined and utilized in many earlier studies. It has been found that the LFDFT predictions are in excellent agreement with the intermediate coupling model, as shown in Table II. LFDFT is a recently available computational model in the ADF program package. For details about calculation of core-electron excitation, please see Ref. [50].

One final note about the theoretical approach before going on to a discussion of the experimental details: A cluster model as utilized here may produce a small set of states corresponding to the point group symmetry of the central atom, but finite solid samples will have bands. It is commonly understood that the individual states produced in cluster calculations will interact with those from other sites and produce bands. The advantage of the cluster model is the application of the electric dipole transition rules to the point group symmetry of the central atom. From the previous success of Cowan's code [23–26], the dominance of local symmetry in the spectroscopic transitions is very clear. To reiterate, an atomic cluster model is being used, so technically speaking, Kohn-Sham molecular orbitals are the result. However, given the localized properties of the $5f$ electronic structure, the approximation via molecular orbitals is also appropriate.

TABLE II. The LFDFT BR predictions are compared with those of the intermediate coupling model (second column). The LFDFT includes both atomic calculations for various ionizations (e.g., 4+) and $5f$ occupancies (e.g., $5f^0$), as well as the cluster results. The charge and electron configuration are shown for each case in parentheses. The values of these shown for the clusters are the ionic limits, not the actual values resulting from the calculations.

BR comparison $5f$ occupation	Intermediate coupling model BR	Atomic Th calculations BR	Atomic U calculations BR	Atomic Pu calculations BR	ThO_8^{12-} BR	UO_8^{12-} BR	PO_8^{12-} BR
$n=0$	0.59	0.58 (4+, $5f^06d^07s^07p^0$) 0.59 (0, $5f^06d^27s^27p^0$)	0.58 (6+, $5f^06d^07s^07p^0$)		0.58 (4+, $5f^06d^07s^07p^0$)		
$n=1$	0.63		0.62 (5+, $5f^16d^07s^07p^0$)				
$n=2$	0.68	0.67 (4+, $5f^26d^07s^07p^0$)	0.67 (6+, $5f^26d^07s^07p^0$)			0.67 (4+, $5f^26d^07s^07p^0$)	
$n=3$	0.72	0.72 (3+, $5f^36d^07s^07p^0$) 0.72 (1+, $5f^36d^07s^27p^0$)	0.72 (5+, $5f^36d^07s^07p^0$)				
$n=4$	0.76			0.75 (4+, $5f^46d^07s^07p^0$)			0.75 (4+, $5f^46d^07s^07p^0$)
$n=5$	0.82			0.79 (3+, $5f^56d^07s^07p^0$)			
$n=6$	0.93						

The experiments were performed at the Stanford Synchrotron Radiation Lightsource (SSRL) at the Stanford Linear Accelerator Center in Menlo Park, CA [44,55], and the Atomic Weapons Establishment (AWE) in Aldermaston, UK [37–39]. The SSRL investigations were HERFD variants of XAS, where an electron is moved from a $3d$ core level into an unoccupied $5f$ state just above the Fermi level or conduction band minimum. HERFD is of significantly improved resolution relative to conventional XAS, with bandpass of $\sim$0.8 eV [44,55]. At AWE, the IPES experiments were carried out at a photon energy of 9.7 eV and a bandpass of 1 eV [37–39]. In IPES, an electron beam impinges upon the sample, and the electron emits a photon as it transitions into an empty $5f$ state near the Fermi level or conduction band minimum. These experiments are discussed in further detail elsewhere [37–39,44,55]. Details of the Chauvet and Baptist experiment can be found in their publication [40].

Following Kvashnina *et al.* [41], the HERFD data described in this paper were generated in experiments that were variants of resonant inelastic x-ray scattering (RIXS). These experiments provide a mechanism for higher-resolution versions of conventional XAS, circumventing the usual limitations caused by conventional detection and lifetime broadening. In general, the high-resolution variant is associated with partial fluorescence yield (PFY) detection. The PFY XAFS spectra are from a cut of the whole RIXS plane. The U $M_{4,5}$ PFY measurements were made at emission energies of $\sim$3.3 and 3.2 keV, respectively. The theoretical modeling of this is based upon the assumption that this PFY decay is a good approximation to total absorption. The theory produced spectral distributions of allowed transitions that were in these ranges, agreeing with the experimental energies [$h\nu(M_4) = 3726$ eV, $h\nu(M_5) = 3552$ eV] to within $\sim$15 eV.

III. RESULTS AND DISCUSSION

To discuss the total DOS and compare the spectral simulations to the IPES/Bremsstrahlung isochromat spectrum (BIS) measurements, both the simulated and experimental HERFD spectra need to be put on a single energy scale. To do this, the energy of the M_5 peak will be set to zero and the M_4 positioned relative to it using the shared transitions into the $5f_{5/2}$ manifold. The relative intensities within the spectral simulations will be retained. The relative intensities in the HERFD experiment will be based upon a normalization using extended x-ray absorption fine structure (EXAFS) and then scaled with the known BR. All of this will be discussed below.

To begin, consider Fig. 1 again. The LFDFT calculations produce an array of number pairs, representing intensity and energy. To convert this array into a simulated spectrum, each data point is convolved with a Lorentzian function of full width at half maximum (FWHM) of $2g$ and then summed, producing a plot of intensity vs energy. Other peak shapes, such as the asymmetric Doniach-Sunjic [56] were also tried with similar results, but the Lorentzian was chosen because of its simplicity and consistency with lifetime broadening. Subsequently, the M_5 spectrum was aligned such that its peak was at an energy of zero, and the integrated M_5 intensity was set to unity. The intensity of the M_4 spectrum was scaled identically to the M_5 spectrum, retaining the correct BR. The energy of the M_4 was shifted so that the M_4 $3d_{3/2} \rightarrow 5f_{5/2}$ peak was at the same energy as the M_5 $3d_{5/2} \rightarrow 5f_{5/2}$ peak. This alignment will be discussed in further detail below. (The scaling and alignment in the experimental spectra are done using EXAFS, as described elsewhere [44]. EXAFS is a component of experimental XAS spectra at higher energies and a manifestation of electron scattering off of neighboring atoms

[44,57].) The dashed gray plots in Fig. 1 show the result of this process for $g = 0.01$ eV, a value which provides only miniscule broadening relative to the natural distribution of energies from the LFDFT. This natural distribution in uranium dioxide reflects the effects of total angular momentum coupling between the $3d$ hole and the $5f$ electrons and the application of coulombic repulsion. It will be seen that the widths of the overall spectra are, to a very large extent, determined by the angular momentum coupling with the smallest widths found in Th, where the near zero $5f$ population precludes strong angular moment coupling effects. There is a crystal or ligand field effect also, but it is smaller than the total angular momentum coupling effect except in special cases, as will be addressed below. This natural distribution is reasonable and expected, but it is insufficient to explain the spectral observations in HERFD. To get agreement between the simulated and experimental spectra, it is necessary to apply larger g values. For the M_4 spectrum, $g_4 = 0.25$ and $FWHM_4 = 0.5$ eV ($FWHM = 2g$). For the M_5 spectrum, a substantially larger value is required: $g_5 = 1$ eV and $FWHM_5 = 2$ eV. A difference in broadening for HERFD M_4 and M_5 spectra is not unreasonable: Conventional, lower-resolution XAS also has a history of level-specific widths [24–26]. It is also of significant interest that the natural distributions of the M_4 and M_5 simulated spectra are so different, reflecting the differences in angular momentum coupling between that of two $5f_{5/2}$ electrons vs that between a $5f_{5/2}$ and a $5f_{7/2}$ electron.

At this point, it is necessary to examine again the issues of scaling and alignment. Consider the results shown in Fig. 2, for thorium. There are three sets of Th data included: ThO_8^{12-} cluster, atomic Th^{4+}, and atomic Th^{4+} in the jj limit. For all three cases, the Th atom has lost all four valence electrons (approximately for ThO_8^{12-} cluster), with a configuration of $(6d7s7p)^0 5f^0$. Thus, the $3d$-$5f$ angular momentum coupling in the final state will be very limited. This leads to a situation where the crystal or ligand field effects will be more obvious. However, first consider the Th^{4+} jj case, as shown in panels (b) and (c) of Fig. 2. Note that the y axis, intensity, is a log scale, to help with the observation of weaker peaks. For Th^{4+} jj, there are only three peaks, corresponding to the electric dipole transitions of M_4 $3d_{3/2} \rightarrow 5f_{5/2}$, M_5 $3d_{5/2} \rightarrow 5f_{5/2}$, and M_5 $3d_{5/2} \rightarrow 5f_{7/2}$. Note that the two M_5 peaks have the correct intensity ratio of $(\frac{4}{15})/(\frac{16}{3}) = 5\%$ [58,59]. The M_4 spectrum is positioned in energy space by aligning the M_4 $3d_{3/2} \rightarrow 5f_{5/2}$ with the M_5 $3d_{5/2} \rightarrow 5f_{5/2}$ because both go into the $5f_{5/2}$ manifold. For the self-consistent calculations of atomic Th^{4+} and the ThO_8^{12-} cluster, the weaker M_5 peaks shift and change intensity, but there remain peaks that can be assigned as M_5 $3d_{5/2} \rightarrow 5f_{5/2}$ which can be used for alignment of the M_4 spectrum. This same procedure was also used for the UO_8^{12-} and PuO_8^{12-} clusters. The alignment for ThO_8^{12-} is shown in panel (a) of Fig. 2.

Returning to the issue of crystal/ligand field splitting, it is possible to see the effect of going from the spherical symmetry of the Th^{4+} to the octahedral symmetry of the ThO_8^{12-} cluster in the M_4 peaks of Fig. 2. Here, a single peak with intensity of ~0.7 is split into two peaks of intensity of ~0.5 and 0.2, approximating the splitting ratio of 3:2:1 expected from group theory [44,60,61]. Of course, it is not
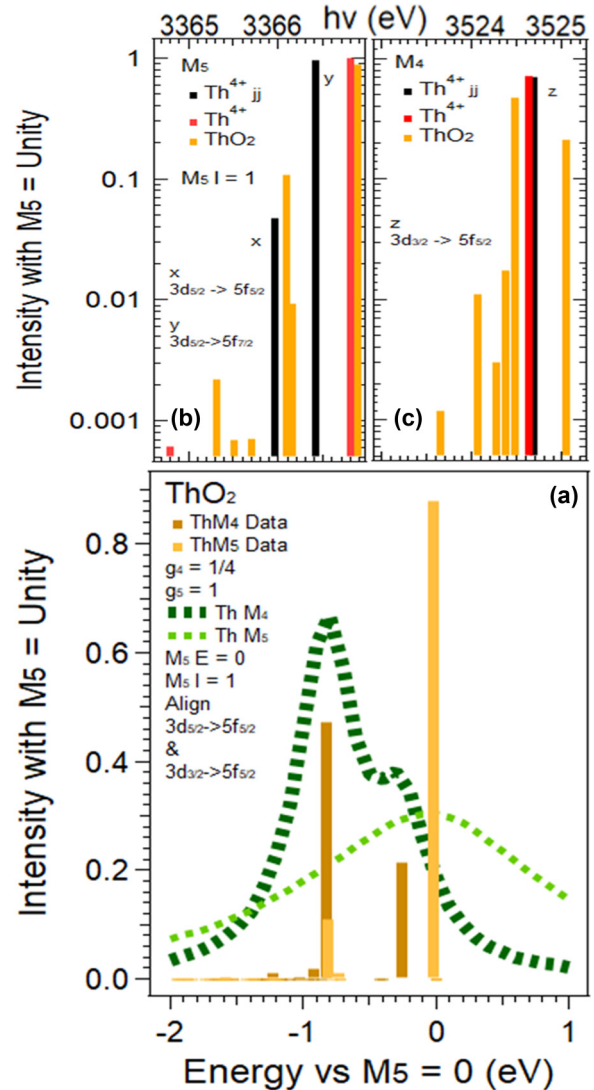

FIG. 2. (a) The ThO_2 computational data and simulated spectral data, illustrating the alignment of the $3d_{5/2} \rightarrow 5f_{5/2}$ and $3d_{3/2} \rightarrow 5f_{5/2}$ peaks. (b) and (c) The M_5 and M_4 computational data for the Th^{4+} jj, Th^{4+} atomic, and ThO_2 cluster. Note the results of the octahedral/cubic splitting of the Th^{4+} in the ThO_8^{12-} results, with I peak becoming two peaks, with intensity ratios of ~0.7 : ~0.5 : ~0.2, roughly the same as that from group theory: Sph : Oct1 : Oct2 = 3:2:1. See text and legends for more detail.

quite as simple as that: There are other, weaker features scattered about in both the M_4 and M_5 distributions for ThO_8^{12-}. Nevertheless, the crystal/ligand field splitting does occur and persists into the simulated M_4 spectrum shown in panel (a) of Fig. 2, using $g_4 = \frac{1}{4}$ eV and $g_5 = 1$ eV, following the UO_2 results. This simulated spectrum is very similar to the experimental M_4 HERFD spectrum of ThO_2 reported by Butorin *et al.* [62], as shown in panel (a) of Fig. 3, validating both the simulation and assertion of crystal field splitting. An interesting point here is that the broader M_5 peak is overlapping the shoulder of the M_4 peak, even for this case with minimal total angular momentum effects. The impact of this overlap will be further discussed below.
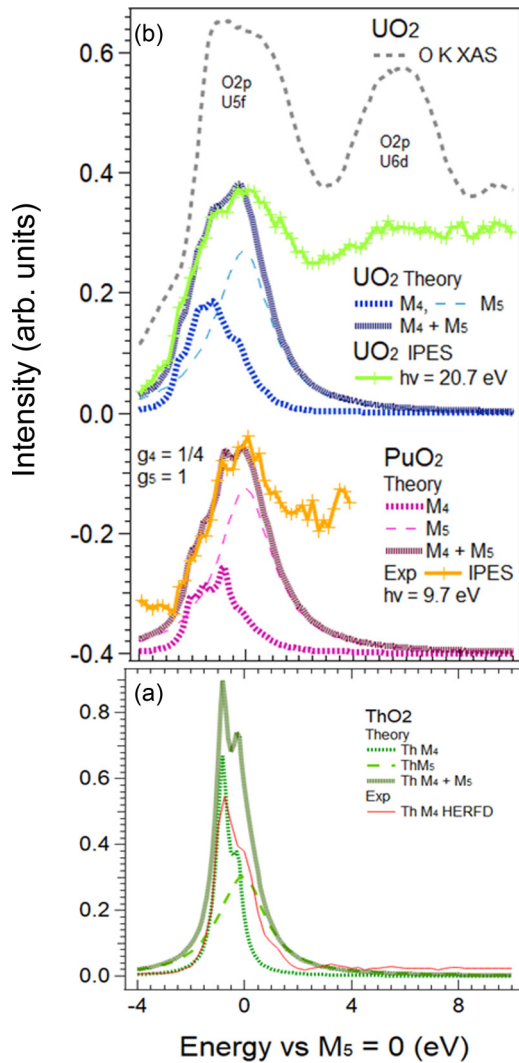
FIG. 3. A comparison of the results for UO_2, PuO_2, and ThO_2. (a) The simulated ligand field density functional theory (LFDFT) M spectra and their sum for the ThO_8^{12-} cluster. Also included is the earlier experimental M_4 high-energy-resolution fluorescence detection (HERFD) of ThO_2 from Butorin *et al.* [62], with permission. Note the high level of agreement, the absence of broadening from angular momentum coupling, and the presence of crystal field splitting in both the theory and experimental M_4 spectra. See the text for detail. (b) A comparison of inverse photoelectron spectroscopy (IPES) and simulated HERFD of UO_2 and PuO_2, as well as the O K (1s) x-ray absorption spectroscopy (XAS) of UO_2 [67]. The UO_2 IPES data are from Chauvet and Baptist [30], at an excitation energy of 20.7 eV. Note the two peaks, assigned as U $5f$ and U $6d$, in agreement with the two peaks in the UO_2 XAS spectrum. The U $6d$ is at 4.5 eV in both XAS and IPES of UO_2. The spectra have been aligned at thresholds. The energy scale is from the spectral calculations, where the center of the M_5 peak is set to zero and the M_4 peak is aligned using the common transitions into the $5f_{5/2}$ unoccupied density of states (UDOS). This process is described in the text.

In earlier studies [44,63,64], it was argued that, because XAS is governed by strong electric dipole selection rules, the HERFD XAS $3d \rightarrow 5f$ measurements produce essentially j-specific mappings of the $5f$ unoccupied DOS (UDOS), and

the summing of the M_4 and M_5 spectra should produce an accurate picture of the total $5f$ UDOS. The assertion that the electric dipole selection rules govern this spectroscopy is supported by the success of the intermediate coupling model in predicting the spectral intensities measured in U, Pu, and other actinides [24–26]. The claim of j specificity is based upon a single particle model for the $d \rightarrow 5f$ transitions that predicts that the M_4 transitions will be solely into $5f_{5/2}$, and the M_5 transitions will be strongly dominated by transitions into $5f_{7/2}$ [44,58,59]. (That is the 5% peak ratio discussed above.) Empirical comparisons of (1) the UO_2 HERFD sum with the UO_2 BIS produced substantial agreement but was limited by the resolution of the BIS data, and (2) a model based upon the Th BIS with several samples across the early actinides showed strong agreement [63,64].

Here, this test is again applied but in a far more stringent and extensive fashion. For UO_8^{12-} and PuO_8^{12-} clusters, the LFDFT calculations were used to produce M_4 and M_5 spectra, which were then summed. These sums were then compared with the IPES of UO_2 [25] and PuO_2 [23]. These results are shown in Fig. 3. While the PuO_2 IPES is from Roussel [38], the UO_2 results are from Chauvet and Baptist [40] and are consistent with many other IPES/BIS [37,39,44,65,66] and other spectroscopic measurements [67]. (BIS is a high-energy variant of IPES.)

Note the remarkable agreement between the sum of the M_4 and M_5 theory curves and the measured IPES for both UO_2 and PuO_2, both in Figs. 1 and 3. This includes the fine structure in the leading edge. From the LFDFT calculations, it is understood that this fine structure comes from the angular momentum coupling, which is dependent upon the $5f$ occupation number n. Both the HERFD and IPES should have angular momentum coupling from the $5f^{n+1}$ electrons in the final state. However, the HERFD also has the possibility for coupling with the $3d$ hole. The strong similarity of the M HERFD and the IPES indicates that the $3d$ core hole coupling is not effective, although the effect can be seen in $5d$ hole–$5f$ electron cases, i.e., $O_{4,5}$ XAS [22,24]. The results for both UO_2 and PuO_2 in Fig. 3(b) are substantially wider than the corresponding ThO_2 results in Fig. 3(b), owing to the larger angular momentum coupling in the U and Pu than Th.

Finally, in the past, there was some concern that IPES would not be sensitive to the $5f$ states at lower photon energies, based upon cross-section dependencies on the photon energy [68]. However, there are several factors that indicate that this concern is not correct. First, extensive spectroscopic studies of UO_2 with x-ray emission spectroscopy (XES), resonant IPES, and XAS all indicate that the O $2p$-$5f$ manifold is near the conduction band minimum and the O $2p$-$6d$ manifold is ~5 eV above that, as shown with the O K XAS spectrum form UO_2, in Fig. 3 [66,67,69]. Second, the extensive IPES studies of Chauvet and Baptist [40] at a range of photon energies ~20 eV indicate that the lower-energy IPES is consistent with the higher-energy BIS ($hv = 1487$ eV) of Baer and Schoenes [65], exhibiting a large peak near the UO_2 conduction band threshold associated with the U $5f$ states. Third, Chauvet and Baptist [40] observe a weaker peak at slightly higher energy, particularly at the lowest photon energies, which is in quantitative agreement of the placement of the O $2p$-U $6d$ manifold in the O K XAS.

Thus, globally, excellent agreement between the LFDFT sum and the IPES is shown in Figs. 1 and 3. It may be that the PuO_2 is showing an uptick at the highest energies, corresponding to the onset of the Pu $5f$-O $2p$ manifold. Overall, the IPES spectral shape and size are dominated by the lifetime-broadened $5f_{7/2}$ contribution. However, the real test is in the leading edge of the IPES, dominated by the $5f_{5/2}$ contribution, illustrated in Fig. 1. Again, clearly, each bit of structure in the IPES is replicated in the LFDFT calculations. This is a tremendous success for the modeling of simulated spectra by LFDFT, (1) demonstrating the validity of the LFDFT approach, (2) explaining the origins of the spectral features in HERFD and IPES, and (3) confirming the assertion that HERFD measures the j-specific $5f$ UDOS.

It is useful to remember that both XAS and IPES are electric-dipole-driven processes, connecting to the $5f$ states. In XAS, the relationship is particularly simple, with transitions between the spherically symmetric but spin-orbit split core levels and the similarly spherically symmetric but spin-orbit split $5f$ states. In IPES and BIS, the incoming electron beam can be thought of in terms of a plane-wave state [56], which can then be separated into the $m = 0$ components of the various spherical harmonics. The incoming plane wave, particularly at normal incidence, can be expected to retain many of the same selection rule and cross-section effects as the core level. Hence, the two measurements are not as dissimilar as they first seem to be.

At this point, there are several important observations. (1) LFDFT using AcO_8^{12-} clusters can accurately simulate both the HERFD and IPES of actinide dioxides. (2) The HERFD does produce a j-specific measure of the $5f$ UDOS. (3) Generally, the HERFD peak shape is driven by total angular momentum coupling, with a smaller crystal/ligand field contribution, broadened by lifetime effects. (4) The sum of the M_4 and M_5 HERFD produces an accurate measure of the total $5f$ DOS. (5) Globally, the IPES of the early actinides is dominated by the many unoccupied states of the $5f_{7/2}$ UDOS, broadened by some sort of lifetime effect. (6) The detailed information in IPES is in the leading edge and corresponds to the $5f_{5/2}$ UDOS. (7) The most efficacious approach to probing $5f$ electronic structure in the early actinides is through a combination of HERFD XAS, XES, and IPES. Traditional approaches based upon photoelectron spectroscopy are limited by the small $5f$ occupation [70] and weak dispersion and the absence of strongly varying spectra structure [71,72]. The unoccupied $5f$ manifolds contain much more information. HERFD XAS and IPES provide two powerful ways to probe the $5f$ UDOS. HERFD XAS and XES [48] allow the j-specific interrogation of the unoccupied and occupied $5f$ DOS, respectively. Further information concerning related spectroscopies of UO_2 can be found in Refs. [73] and [74].

IV. SUMMARY AND CONCLUSIONS

(1) Consistent with the success of Cowan's code to explain the BRs in conventional XAS, total angular momentum coupling plays a near dominant role in both HERFD and IPES/XES. Except for the special case of Th with $n = 0$, total angular momentum coupling, with broadening from either instrumental or lifetime contributions, generates the asymmetric line shape that has been observed in both HERFD and IPES/BIS.

(2) Underlying the broad asymmetric line shapes are the crystal field split unoccupied states of the $5f$ manifolds. In cluster calculations, these will appear as discrete states, but in the solids, these states will broaden into bands.

(3) In the early actinide dioxides, with the $5f_{7/2}$ manifold almost completely empty, the major effect is the generation of a large and somewhat asymmetric peak in the M_5 HERFD spectrum and the higher-energy side of the IPES/BIS peak. The broadening here is mainly due to a larger lifetime broadening in the $5f_{7/2}$ manifold than in the $5f_{5/2}$ manifold, consistent with the $5f_{7/2}$ manifold being at a higher energy than the $5f_{5/2}$ manifold.

(4) In the early actinide dioxides, the major changes are in the M_4 HERFD spectrum and the leading (low energy) edge of the IPES/BIS. For ThO_2 with $n = 0$, the angular momentum coupling effects collapse, and the crystal field splitting can be observed in the M_4 HERFD spectrum. In UO_2 and PuO_2, the fine structure in the leading edge of the IPES is in near perfect agreement with the predictions of the spectral simulations.

(5) Within the limitations imposed by angular momentum coupling and experimental broadening, the following hypotheses have been confirmed: (a) the M_4 HERFD spectrum is a measure of the $5f_{5/2}$ UDOS; (b) the M_4 HERFD spectrum is a measure of the $5f_{7/2}$ UDOS; and (c) the sum of the M_4 and M_5 spectra is a measure of the total $5f$ UDOS, consistent with the measurements from IPES/BIS.

A final caveat: This analysis of actinide dioxides applies to high-symmetry, localized $5f$ systems with single bonds. Effects such as $5f$ delocalization [25,72] and multiple bond structures [41,42], as in uranyls [63,64], could manifest behavior that is different.

[1] S. S. Hecker, MRS Bull. **26**, 672 (2001).

[2] S. J. Zinkle and G. S. Was, Acta Mater. **61**, 735 (2013).

[3] Nuclear Energy Institute, Nuclear shares of electricity generation, http://www.world-nuclear.org/info/nshare.html.

[4] S.-W. Yu and J. G. Tobin, J. Electron Spectrosc. Relat. Phenom. **187**, 15 (2013), and references therein.

[5] I. L. Pegg, Phys. Today **68**(2), 33 (2015).

[6] J. G. Tobin, A. M. Duffin, S.-W. Yu, R. Qiao, W. L. Yang, C. H. Booth, and D. K. Shuh, J. Vac. Sci. Technol. A **35**, 03E108 (2017).

[7] S.-W. Yu and J. G. Tobin, J. Vac Sci. Tech. A **29**, 021008 (2011).

[8] J. G. Tobin, B. W. Chung, R. K. Schulze, J. Terry, J. D. Farr, D. K. Shuh, K. Heinzelman, E. Rotenberg, G. D. Waddill, and G. van der Laan, Phys. Rev. B **68**, 155109 (2003).

[9] J. Terry, R. K. Schulze, J. Lashley, J. D. Farr, T. Zocco, K. Heinzelman, E. Rotenberg, D. K. Shuh, G. Van der Laan, and J. G. Tobin, Surf. Sci. Lett. **499**, L141 (2002).

[10] K. T. Moore, G. van der Laan, J. G. Tobin, B. W. Chung, M. A. Wall, and A. J. Schwartz, Ultramicroscopy **106**, 261 (2006).

[11] B. W. Veal, D. J. Lam, H. Diamond, and H. R. Hoekstra, Phys. Rev. B **15**, 2929 (1977).

[12] B. W. Veal and D. J. Lam, Phys. Rev. B **10**, 4902 (1974).

[13] A. B. Shick, J. Kolorenc, L. Havela, T. Gouder, and R. Caciuffo, Phys. Rev. B **89**, 041109(R) (2014).

[14] J. Kolorenc, A. B. Shick, and A. I. Lichtenstein, Phys. Rev. B **92**, 085125 (2015).

[15] J. Kolorenč and K. O. Kvashnina, MRS. Adv. **3**, 3143 (2018).

[16] I. D. Prodan, G. E. Scuseria, and R. L. Martin, Phys. Rev. B **76**, 033101 (2007).

[17] X.-D. Wen, R. L. Martin, L. E. Roy, G. E. Scuseria, S. P. Rudin, E. R. Batista, T. M. McCleskey, B. L. Scott, E. Bauer, J. J. Joyce, and T. Durakiewicz, J. Chem. Phys. **137**, 154707 (2012).

[18] https://en.wikipedia.org/wiki/Thorium_dioxide.

[19] https://en.wikipedia.org/wiki/Uranium_dioxide.

[20] https://en.wikipedia.org/wiki/Plutonium(IV)_oxide.

[21] C. F. Molen and R. D. White, *Properties of Plutonium Oxide, Part II* (The Dow Chemical Company, Golden, 1967).

[22] H. Ramanantoanina, G. Kuri, C. Daul, and J. Bertscha, Phys. Chem. Chem. Phys. **18**, 19020 (2016).

[23] G. van der Laan and B. T. Thole, Phys. Rev. B **53**, 14458 (1996).

[24] G. van der Laan, K. T. Moore, J. G. Tobin, B. W. Chung, M. A. Wall, and A. J. Schwartz, Phys. Rev. Lett. **93**, 097401 (2004).

[25] J. G. Tobin, K. T. Moore, B. W. Chung, M. A. Wall, A. J. Schwartz, G. van der Laan, and A. L. Kutepov, Phys. Rev. B **72**, 085109 (2005).

[26] J. G. Tobin, S.-W. Yu, C. H. Booth, T. Tyliszczak, D. K. Shuh, G. van der Laan, D. Sokaras, D. Nordlund, T.-C. Weng, and P. S. Bagus, Phys. Rev. B **92**, 035111 (2015).

[27] Y. Savrasov, G. Kotliar, and E. Abrahams, Nature (London) **410**, 793 (2001).

[28] J. H. Shim, K. Haule, and G. Kotliar, Nature (London) **446**, 513 (2007).

[29] E. Runge, P. Fulde, D. V. Efremov, N. Hasselmann, and G. Zwicknagl, Phys. Rev. B **69**, 155110 (2004).

[30] D. V. Efremov, N. Hasselmann, E. Runge, P. Fulde, and G. Zwicknagl, Phys. Rev. B **69**, 115114 (2004).

[31] F. Pollmann and G. Zwicknagl, Phys. Rev. B **73**, 035121 (2006).

[32] J. J. Joyce, J. M. Wills, T. Durakiewicz, M. T. Butterfield, E. Guziewicz, J. L. Sarrao, L. A. Morales, A. J. Arko, and O. Eriksson, Phys. Rev. Lett. **91**, 176401 (2003).

[33] K. Gofryk, J.-C. Griveau, P. S. Riseborough, and T. Durakiewicz, Phys. Rev. B **94**, 195117 (2016).

[34] M. Janoschek, B. Chakrabarti P.Das, D. L. Abernathy, M. D. Lumsden, J. M. Lawrence, J. D. Thompson, G. H. Lander, J. N. Mitchell, S. Richmond, M. Ramos, F. Trouw, J.-X. Zhu, K. Haule, G. Kotliar, and E. D. Bauer, Sci. Adv. **1**, e1500188 (2015).

[35] M. Janoschek, G. Lander,J. M. Lawrence, E. D. Bauer, J. C. Lashley, M. Lumsden, D. L. Abernathy, and J. D. Thompson, Proc. Natl. Acad. Sci. USA **114**, E268 (2017).

[36] S. W. Yu, J. G. Tobin, and P. Söderlind, J. Phys.: Condens. Matter **20**, 422202 (2008).

[37] P. Roussel, P. Morrall, and S. J. Tull, J. Nucl. Matl. **385**, 53 (2009).

[38] P. Roussel, J. Electron Spectrosc. Relat. Phenom. **246**, 147030 (2021).

[39] P. Roussel, A. J. Bishop, and A. F. Carley, Surf. Sci. **714**, 121914 (2021).

[40] G. Chauvet and R. Baptist, Solid State Commun. **43**, 793 (1982).

[41] K. O. Kvashnina, S. M. Butorin, P. Martin, and P. Glatzel, Phys. Rev. Lett. **111**, 253002 (2013).

[42] T. Vitova, I. Pidchenko, D. Fellhauer, P. S. Bagus, Y. Joly, T. Pruessmann, S. Bahl, E. Gonzalez-Robles, J. Rothe, M. Altmaier, M. A. Denecke, and H. Geckeis, Nat. Commun. **8**, 16053 (2016).

[43] K. O. Kvashnina, H. C. Walker, N. Magnani, G. H. Lander, and R. Caciuffo, Phys. Rev. B **95**, 245103 (2017).

[44] J. G. Tobin, S. Nowak, C. H. Booth, E. D. Bauer, S.-W. Yu, R. Alonso-Mori, T. Kroll, D. Nordlund, T.-C. Weng, and D. Sokaras, J. Electron Spectrosc. Relat. Phenom. **232**, 100 (2019).

[45] M. Pepper and B. E. Bursten, Chem. Rev. **91**, 719 (1991).

[46] S. K. Singh, C. J. Cramer, and L. Gagliardi, Inorg. Chem. **59**, 6815 (2020).

[47] L. Gagliardi, Int. J. Quantum Chem. **111**, 3302 (2011).

[48] H. Chermette, Coord. Chem. Rev. **178–180**, 699 (1998).

[49] M. E. Casida and M. Huix-Rotllant, Annu. Rev. Phys. Chem. **63**, 287 (2012).

[50] H. Ramanantoanina, J. Chem. Phys. **149**, 054104 (2018).

[51] G. te Velde, F. M. Bickelhaupt, E. J. Baerends, C. Fonseca Guerra, S. J. A. van Gisbergen, J. G. Snijders, and T. Ziegler, J. Comput. Chem. **22**, 931 (2001).

[52] P. J. Stephens, F. J. Devlin, C. F. Chabalowski, and M. J. Frisch, J. Phys. Chem. **98**, 11623 (1994).

[53] E. Van Lenthe and E. J. Baerends, J. Comput. Chem. **24**, 1142 (2003).

[54] E. van Lenthe, E. J. Baerends, and J. G. Snijders, J. Chem. Phys. **99**, 4597 (1993).

[55] S. H. Nowak, C. Schwartz, R. Armenta, A. Gallo, D. Day, S. Christensen, R. Alonso-Mori, T. Kroll, D. Nordlund, T.-C. Weng, and D. Sokaras, Rev. Sci. Instrum. **91**, 033101 (2020).

[56] J. G. Tobin and F. O. Schumann, Surf. Sci. **478**, 211 (2001).

[57] J. G. Tobin, S. Nowak, S.-W. Yu, R. Alonso-Mori, T. Kroll, D. Nordlung, T.-C. Weng, and D. Sokaras, Surf. Sci. **698**, 121607 (2020).

[58] J. G. Tobin, S. Nowak, S.-W. Yu, R. Alonso-Mori, T. Kroll, D. Nordlund, T.-C. Weng, and D. Sokaras, J. Phys. Commun. **4**, 015013 (2020).

[59] J. G. Tobin, S. Nowak, S.-W. Yu, R. Alonso-Mori, T. Kroll, D. Nordlund, T.-C. Weng, and D. Sokaras, Appl. Sci. **10**, 2918 (2020); Erratum, **10**, 4242(E) (2020).

[60] J. G. Tobin, J. Vac. Sci. Technol. A **37**, 031201 (2019).

[61] J. G. Tobin, J. Electron Spectrosc. Relat. Phenom. **194**, 14 (2014).

[62] S. M. Butorin, K. O. Kvashnina, J. R. Vegelius, D. Meyer, and D. K. Shuh, Proc. Natl. Acad. Sci. USA **113**, 8093 (2016).

[63] J. G. Tobin, S. Nowak, S.-W. Yu, P. Roussel, R. Alonso-Mori, T. Kroll, D. Nordlund, T.-C. Weng, and D. Sokaras, J. Vac. Sci. Tech. A **39**, 043205 (2021).

[64] J. G. Tobin, S. Nowak, S.-W. Yu, P. Roussel, R. Alonso-Mori, T. Kroll, D. Nordlund, T.-C. Weng, and D. Sokaras, J. Vac. Sci. Tech. A **39**, 066001 (2021).

[65] Y. Baer and J. Schoenes, Solid State Commun. **33**, 885 (1980).

[66] S.-W. Yu, J. G. Tobin, J. C. Crowhurst, S. Sharma, J. K. Dewhurst, P. Olalde-Velasco, W. L. Yang, and W. J. Siekhaus, Phys. Rev. B **83**, 165102 (2011).

[67] J. G. Tobin, S.-W. Yu, R. Qiao, W. L. Yang, C. H. Booth, D. K. Shuh, A. M. Duffin, D. Sokaras, D. Nordlund, and T.-C. Weng, Phys. Rev. B **92**, 045130 (2015).

[68] J. J. Yeh and I. Lindau, At. Data Nucl. Data Tables **32**, 1 (1985).

[69] J. G. Tobin and S.-W. Yu, Phys. Rev. Lett **107**, 167406 (2011).

[70] J. G. Tobin, P. Söderlind, A. Landa, K. T. Moore, A. J. Schwartz, B. W. Chung, M. A. Wall, J. M. Wills, R. G. Haire, and A. L. Kutepov, J. Phys. Cond. Matter **20**, 125204 (2008).

[71] J. G. Tobin, S. W. Yu, B. W. Chung, and G. D. Waddill, J. Nucl. Matl. **385**, 31 (2009).

[72] J. G. Tobin, S. Nowak, S.-W. Yu, R. Alonso-Mori, T. Kroll, D. Nordlund, T.-C. Weng, and D. Sokaras, Appl. Sci. **11**, 3882 (2021).

[73] M. Sundermann, G. van der Laan, A. Severing, L. Simonelli, G. H. Lander, M. W. Haverkort, and R. Caciuffo, Phys. Rev. B **98**, 205108 (2018).

[74] R. Caciuffo, G. van der Laan, L. Simonelli, T. Vitova, C. Mazzoli, M. A. Denecke, and G. H. Lander, Phys. Rev. B **81**, 195104 (2010).